nature materials

ARTICLES

PUBLISHED ONLINE: 11 DECEMBER 2017 | DOI: 10.1038/NMAT5050

A sol–gel monolithic metal–organic framework with enhanced methane uptake

Tian Tian[1], Zhixin Zeng[2], Diana Vulpe[1], Mirian E. Casco[3], Giorgio Divitini[4], Paul A. Midgley[4], Joaquin Silvestre-Albero[3], Jin-Chong Tan[2], Peyman Z. Moghadam[1] and David Fairen-Jimenez[1]*

A critical bottleneck for the use of natural gas as a transportation fuel has been the development of materials capable of storing it in a sufficiently compact form at ambient temperature. Here we report the synthesis of a porous monolithic metal–organic framework (MOF), which after successful packing and densification reaches 259 cm^3 (STP) cm^{-3} capacity. This is the highest value reported to date for conformed shape porous solids, and represents a greater than 50% improvement over any previously reported experimental value. Nanoindentation tests on the monolithic MOF showed robust mechanical properties, with hardness at least 130% greater than that previously measured in its conventional MOF counterparts. Our findings represent a substantial step in the application of mechanically robust conformed and densified MOFs for high volumetric energy storage and other industrial applications.

Natural gas (NG), mainly composed of methane, has long been considered as a preferable energy alternative to traditional fossil fuels due to its high hydrogen to carbon ratio and lower CO_2 emissions[1,2]. However, the low energy density of methane compared with traditional fossil fuels restrains its on-board applicability. A long-standing challenge has been to design storage systems that efficiently and safely store methane at a realistic volume and that allow it to be easily extracted at reasonable pressures and temperatures[3]. In 2012, the US Department of Energy (DOE) set the ambitious volumetric storage target for adsorbed natural gas (ANG) to 263 cm^3 (STP) cm^{-3} at room temperature and 65 bar[4], equivalent to the storage capacity of an empty tank at 250 bar—targets which, to this day, have not been met by any conformed material after packing. Since the highest reported values were 180 cm^3 (STP) cm^{-3} (ref. 5), it has so far been unclear whether a material able to reach DOE targets could even be developed. Achieving DOE targets is critical for use in wider vehicular/transportation applications or NG transoceanic shipping.

From all the existing adsorbents, MOFs, obtained by the coordination of metal clusters with organic linkers, are arguably the most promising class of methane storage materials due to their large surface areas and pore volumes[1,6]. MOFs are one of the most exciting advances in recent porous materials science, with currently 75,600 different structures in the Cambridge Structural Database[7]. They symbolize the beauty of porous coordination polymers and the possibility of modifying their individual chemical and physical properties. From all the multiple structural possibilities, a careful examination of 137,953 hypothetical[8,9] and over 4,700 already-synthesized[8] MOF structures using molecular simulations have predicted a maximum methane adsorption capacity of 267 cm^3 (STP) cm^{-3}. However, volumetric capacities obtained computationally are almost always calculated using the ideal single-crystal density of MOFs and, due to the existence of packing issues in real scenarios, these values are, in the best case, only theoretical[10,11].

In a recent work, Peng *et al.*[5] studied experimentally the effect of MOF shaping and densification on methane adsorption. They identified HKUST-1 [$Cu_3(BTC)_2(H_2O)_3$] (BTC = 1,3,5-benzenetricarboxylate) as the only material capable of achieving the volumetric DOE target—again, using the theoretical crystal density of the MOF (that is, 0.883 g cm^{-3})—and with a maximum uptake of 270 cm^3 (STP) cm^{-3} at 65 bar. However, when HKUST-1 was experimentally packed and densified, the volumetric adsorption capacity was reduced down to 180 cm^3 (STP) cm^{-3} (that is, 35% loss compared to the theoretical maximum value) because of the partial mechanical collapse of the internal pore structure. Densification and pelletization of MOFs is indeed one of the main challenges for MOF applications in industry, since conventional synthesis methods produce MOFs as powders with very low packing density, generally three to four times lower than the theoretical crystal density[12].

In this work, we aimed to determine whether there exists a plausible synthetic protocol for a MOF that would meet the DOE volumetric targets. We used our recent developments in advanced synthesis, engineering and densification of MOFs to produce pure monolithic structures of up to about 1 cm^3 in size without using high pressures or additional binders[12,13]. We focus here on HKUST-1 as the—theoretically—top-performing MOF for methane adsorption synthesized to date.

Sol–gel synthesis of MOFs

The synthesis of the high-density $_{mono}$HKUST-1 described here follows a sol–gel process similar to the synthesis of organic and inorganic aero/xerogels[14–18]. Figure 1 shows the proposed synthetic mechanism followed in this work, the optical image of $_{mono}$HKUST-1, and the powder X-ray diffraction (PXRD) patterns of the samples. After the formation of the crystalline, primary MOF particles at the beginning of the reaction, the mother solution was centrifuged and the resulting densified solid (that is, the gel) was washed to remove unreacted precursors. We found the drying

[1]Adsorption and Advanced Materials (AAM) Laboratory, Department of Chemical Engineering and Biotechnology, University of Cambridge, Philippa Fawcett Drive, Cambridge CB3 0AS, UK. [2]Multifunctional Materials & Composites (MMC) Laboratory, Department of Engineering Science, University of Oxford, Parks Road, Oxford OX1 3PJ, UK. [3]Laboratorio de Materiales Avanzados, Departamento de Química Inorgánica-Instituto Universitario de Materiales, Universidad de Alicante, Ctra. San Vicente-Alicante s/n, E-03080 Alicante, Spain. [4]Electron Microscopy Group, Department of Materials Science and Metallurgy, University of Cambridge, 27 Charles Babbage Road, Cambridge CB3 0FS, UK. *e-mail: df334@cam.ac.uk

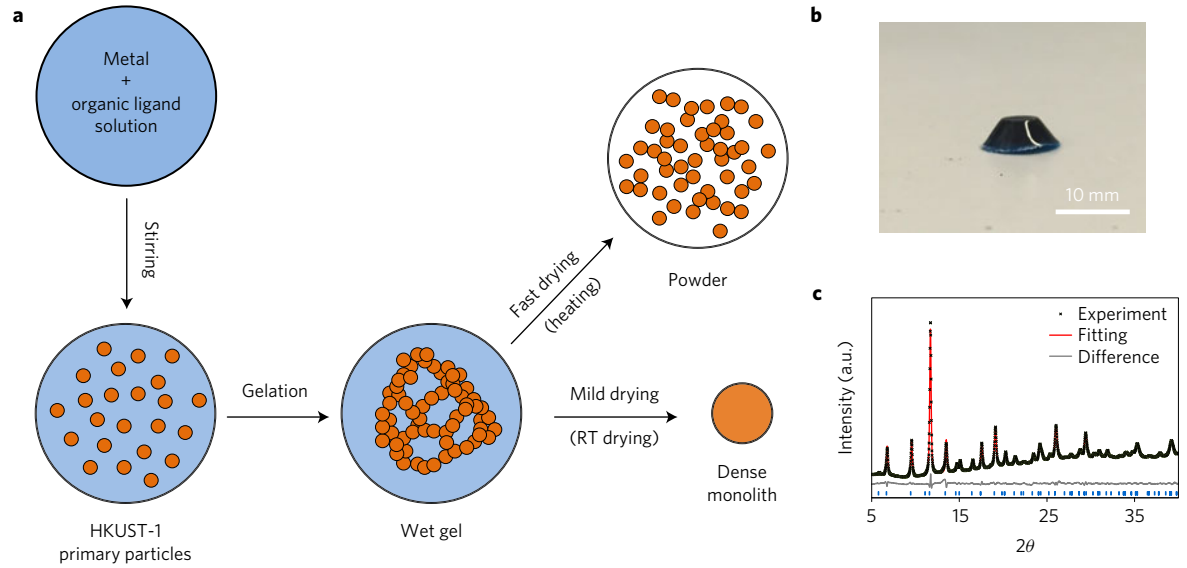

Figure 1 | Schematic representation of monolithic and powder MOF synthesis. a, The synthesis follows a sol–gel process, where a dense monolith is obtained under mild drying conditions whereas powders are obtained when the wet gel is dried at higher temperature or vacuum. **b**, Optical image of the monolithic MOF, $_{mono}$HKUST-1, showing it maintains the shape of the mould where it was prepared. **c**, Comparison of PXRD patterns of $_{mono}$HKUST-1: observed (black symbols), Pawley fitting (red line), and difference (grey line), confirming the successful synthesis of HKUST-1.

temperature to be critical for the final morphology of HKUST-1. On the one hand, if the dense gel was dried at high temperature, the fast removal of the solvent from the interstitial spaces between primary particles does not allow the gel macrostructure to be maintained, and therefore only a powder was obtained (named here $_{powd}$HKUST-1). On the other hand, if the dense gel is dried at mild conditions (for example, room temperature), the retained precursors start nucleating at the interface, experiencing an epitaxial growth within the existing primary particles. In this way, the MOF, a porous coordination polymer, acts as a binder, closely connecting the existing primary particles together, and leading to a dense, glassy-look monolith (Fig. 1b).

Elemental analysis for experimental $_{mono}$HKUST-1 and $_{powd}$HKUST-1 samples did not show any important differences between them and the theoretical composition of hydrated HKUST-1, with about 1 water molecule per Cu atom (Supplementary Table 1). High-resolution PXRD analysis and Pawley fitting showed that the crystalline phase of both $_{mono}$HKUST-1 and $_{powd}$HKUST-1 was the same as the predicted HKUST-1 single crystal (Fig. 1c and Supplementary Fig. 1). No extra crystalline phases were observed, although at this point the existence of amorphous phases inside the MOF primary particles or acting as a binder cannot be discarded. Fourier transform infrared (FTIR) spectroscopy showed essentially identical peaks in both $_{mono}$HKUST-1 and $_{powd}$HKUST-1 samples (Supplementary Fig. 2), indicating that there were no new chemical functionalities in the monolith. A careful examination of transmission electron microscopy (TEM) images showed that the powder sample is formed by an aggregation of primary particles of about 51 nm size (Supplementary Figs 3a and 4), whereas the monolithic sample is made of a continuous phase where the primary particles can no longer be observed (Fig. 2 and Supplementary Fig. 5)—that is, there is no boundary or interphase between primary particles. Electron diffraction also showed the same results for powder and monolithic samples (Supplementary Fig. 6).

We have identified three key factors in the synthesis of the monolithic MOF (ref. 12). First, the primary particles of the monolith need to be small; in our case it is 51 ± 10 nm (Supplementary Fig. 3a). This was also suggested by Horcajada *et al.* when preparing MIL-89 aero/xerogels[19]. Second, the nucleation and crystal growth processes between MOF primary particles during

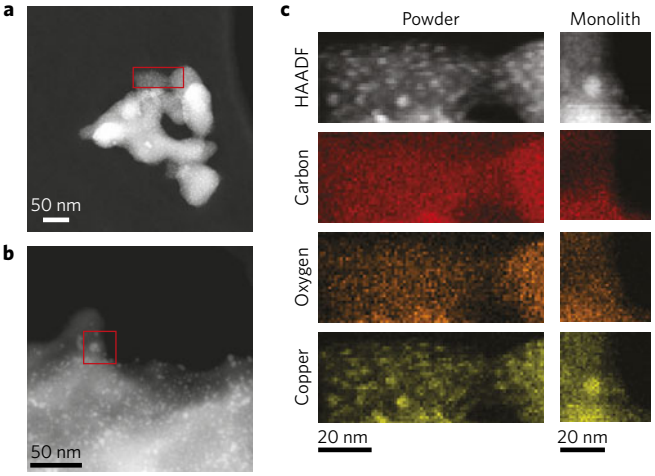

Figure 2 | Transmission electron microscopy images of monolithic and powder MOF samples. a, TEM image of $_{powd}$HKUST-1. **b**, TEM image of $_{mono}$HKUST-1. **c**, Energy-dispersive X-ray spectroscopy (EDX) analysis and elemental maps of the selected areas (red rectangles) from **a** and **b**. HAADF, high-angle annular dark-field.

the drying process need to be fast under the selected conditions. If the conditions are unfavourable, the weak interactions will induce a mismatched growth, resulting in a non-crystalline gel[20]. Third, the drying process needs to be achieved under mild conditions—that is, typically lower than 40 °C and avoiding a vacuum. With a slow drying process, it is possible to avoid the mechanical stress at the vapour–liquid meniscus interface of the solvent inside the porosity, and to get a dense monolithic structure instead of a powdered MOF. To probe the synthesis mechanism, we prepared two additional HKUST-1 samples with larger particle size: 73 ± 18 and 145 ± 60 nm (Supplementary Fig. 3b,c), and then dried the samples at different temperatures in the range from 20 to 80 °C. Supplementary Table 2 shows the effect of particle size and drying temperature on the formation of either the monolithic structure or the powder. We found that samples with a particle size of 51 nm can be successfully dried up to 40 °C to get the monolithic structure.

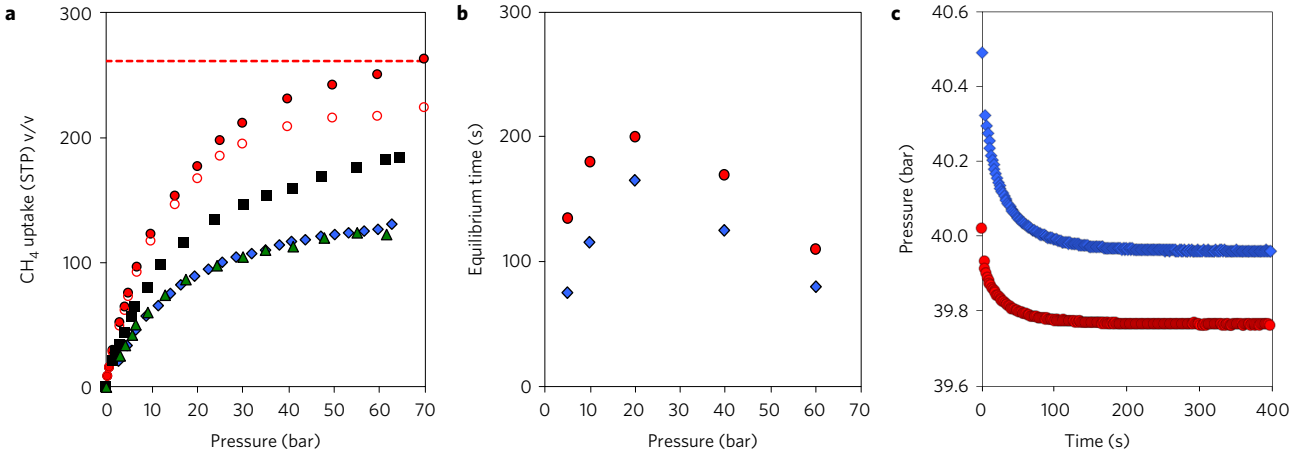

Figure 3 | Gas adsorption in HKUST-1. a, Comparison of absolute volumetric methane adsorption isotherms at 298 K on $_{mono}$HKUST-1 (red filled circles), excess volumetric uptake on $_{mono}$HKUST-1 (red open circles), HKUST-1 pellets under hand packing (blue diamonds), HKUST-1 pellets packed under 27.6 MPa (black squares), and HKUST-1 pellets under 68.9 MPa (green triangles)[5]. The DOE target of 263 cm^3 (STP) cm^{-3} is represented by the red dashed line. **b**,**c**, Equilibrium time of methane adsorption at 298 K as a function of equilibrium pressure (**b**), and decay of pressure with time at 40 bar (**c**), for $_{mono}$HKUST-1 (blue diamonds) and $_{powd}$HKUST-1 (red circles).

Table 1 | BET areas (S_{BET}), micropore volume (W_0), total pore volume (V_{tot}) and bulk density (ρ_b) for $_{mono}$HKUST-1.

Materials	S_{BET}	W_0*	V_{tot}†	ρ_b‡	S_{BET} (vol)	V_{tot} (vol)	CH_4 uptake§	
	$m^2\ g^{-1}$	$cm^3\ g^{-1}$	$cm^3\ g^{-1}$	$g\ cm^{-3}$	$m^2\ cm^{-3}$	$cm^3\ cm^{-3}$	g/g	v/v
$_{mono}$HKUST-1	1,193	0.51	0.52	1.06	1,288	0.56	0.177	259
Peng *et al.*[2]	1,850	0.68	0.78	0.43‖	796	0.33	0.216	130

*Obtained at $P/P_0 = 0.1$; †obtained at $P/P_0 = 0.99$; ‡bulk density quantified by measuring the weight and volume using mercury porosimetry; §total uptake; ‖hand packing density[5].

On the other hand, samples with a particle size of 73 nm can be successfully dried only up to 30 °C, whereas samples with a particle size of 145 nm cannot yield the monolithic structure at any temperature.

Density and porosity of monolithic HKUST-1

During standard activation of $_{mono}$HKUST-1 under heat (120 °C) and vacuum without any extra processing (Supplementary Figs 14 and 15), we found that the sample was able to retain the macroscopic monolithic morphology and shape of the mould (Fig. 1b). Supplementary Fig. 7 shows the SEM images of the monoliths and corresponding $_{powd}$HKUST-1. There is a clear difference in the way the material is packed: $_{powd}$HKUST-1 is a simple agglomeration of particles with a large amount of interstitial space, whereas the $_{mono}$HKUST-1 surface is much more compact and with a minimal amount of interstitial space. The porosity was evaluated using N_2 adsorption at 77 K (Supplementary Fig. 8); it showed a typical Type I isotherm shape, indicative of the microporous character of the monoliths[12]. Table 1 compares the bulk densities, gravimetric and volumetric Brunauer, Emmett and Teller (BET) areas and pore volumes of $_{mono}$HKUST-1 with the HKUST-1 powder samples from Peng and colleagues[5]. The lower gravimetric BET areas compared with previously reported data (that is, in the range of 1,500–1,850 $m^2\ g^{-1}$) (refs 5,21,22) are expected due to the short synthesis time (10 min) and low synthesis temperature (20 °C), similar to other reported nanoscale MOF syntheses such as ZIF-8 (refs 23–25) and MIL-53 (ref. 26). In spite of the lower BET areas, the critical advantage of monolithic MOFs is their high bulk density, and therefore higher volumetric BET areas, pore volumes and adsorption capacities compared to their traditional powdered counterparts. The measured bulk density of $_{mono}$HKUST-1 (that is, 1.06 ± 0.05 $g\ cm^{-3}$, Supplementary Table 3) was higher than the hand packed and, remarkably, than the crystal densities of HKUST (0.430 and 0.883 $g\ cm^{-3}$, respectively). In our case, the bulk density of $_{powd}$HKUST-1 was 0.40 $g\ cm^{-3}$. The larger density of $_{mono}$HKUST-1 is related to the better packing, and to the presence of amorphous, denser phases (Supplementary Figs 10 and 11 and Supplementary Tables 5–7). Supplementary Fig. 9 shows the pore size distributions obtained from mercury porosimetry up to 206 MPa (that is, equivalent to 60 Å). The volumes of mercury intruded for $_{mono}$HKUST-1 and $_{powd}$HKUST-1 were 0.037 and 1.922 $cm^3\ g^{-1}$, respectively. In particular, the volume of mercury intruded for $_{powd}$HKUST-1 comes from the interparticle space rather than any real porosity.

Natural gas adsorption of monolithic HKUST-1

To probe the improved performance of densified MOFs in NG storage, we ran methane adsorption isotherms at room temperature and up to 70 bar (Supplementary Table 4). Figure 3a compares the absolute volumetric adsorption isotherms of methane in $_{mono}$HKUST-1 at 298 K with previous powdered and densified HKUST-1 samples[5]. We also included the 263 cm^3 (STP) cm^{-3} target from DOE for benchmark comparison. The gravimetric uptake is shown in Supplementary Fig. 12 for comparison. It is important to note that the experimentally measured values are excess amounts adsorbed (N_{exc}), which are transformed into absolute uptakes (N_{abs}) by using equation (1):

$$N_{abs} = N_{exc} + \rho V_{pore} \quad (1)$$

where ρ is the density of the gas at the given adsorption pressure and temperature, obtained from the National Institute of Standards and Technology (NIST)[27], and V_{pore} is the pore volume of the adsorbent[28]. Interestingly, the volumetric methane storage capacity of the $_{mono}$HKUST-1 (that is, 259 cm^3 (STP) cm^{-3} at 65 bar) virtually matches the DOE target due to the high bulk density

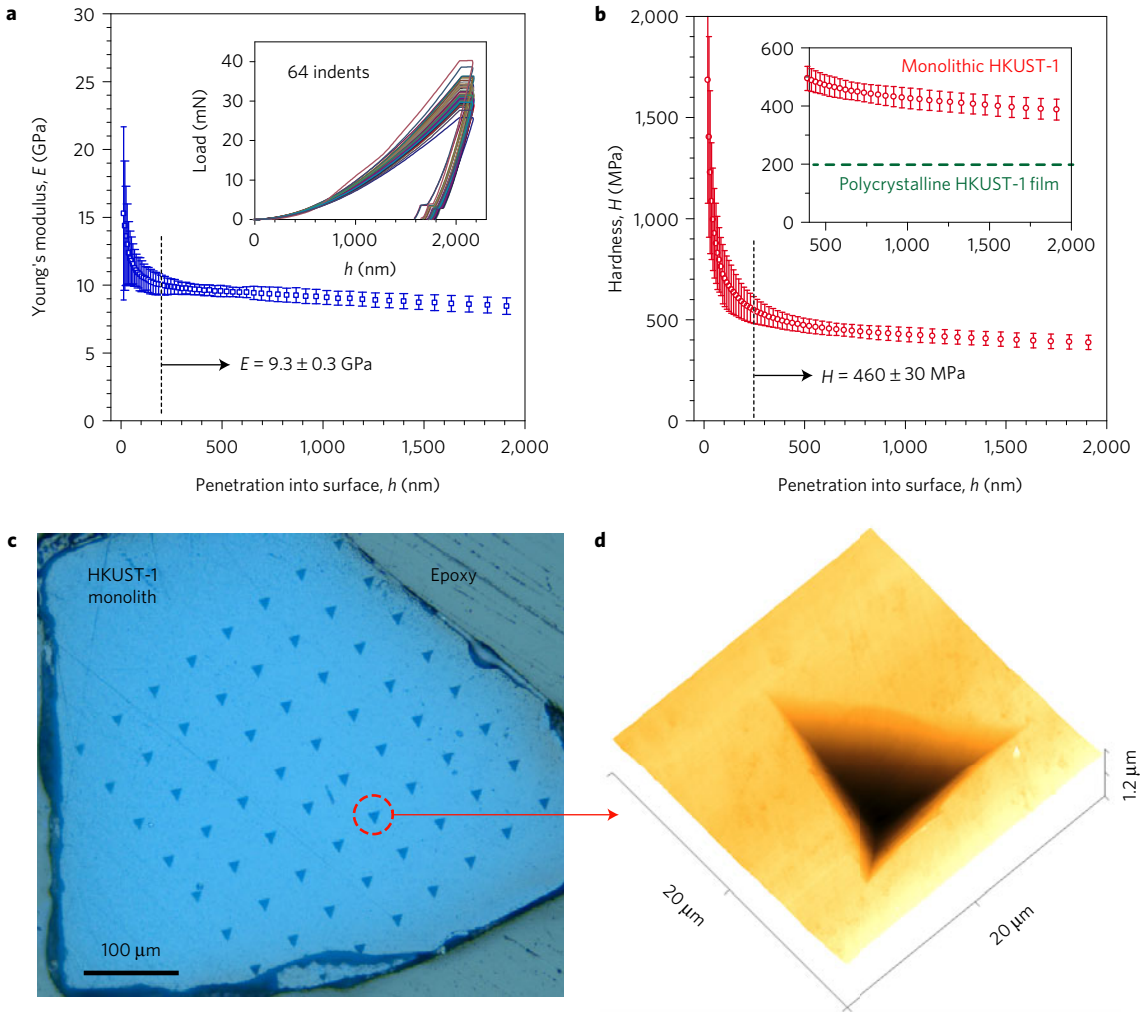

Figure 4 | Nanoindentation on $_{mono}$HKUST-1. a,**b**, Young's modulus and hardness, respectively, as a function of indentation depth on a $_{mono}$HKUST-1 sample. Averaged properties were derived from 60 indents, using penetration depths of 200–2,000 nm, thus ensuring results are free from surface defects and tip calibration artefacts. Error bars are standard deviations calculated from 60 measurements. The inset in **a** shows the load–displacement raw data. The inset in **b** shows the hardness of $_{mono}$HKUST-1 is double that of its conventional polycrystalline counterpart ($H \sim 200$ MPa) (ref. 41). **c**, Optical micrograph showing the array of residual indents, showing no evidence of radial cracking. **d**, AFM profile depicting the 3D topography of a representative indent, showing there is no sign of surface cracking, and thus indicating good mechanical resilience of the monolith.

of the monolithic structure. To the best of our knowledge, this is the first example of an adsorbent—including MOFs but also other traditional porous materials such as activated carbons and zeolites—that can achieve the DOE target after successful packing[11]. Remarkably, the high methane adsorption capacity of $_{mono}$HKUST-1 is very close to the theoretical, but unachievable volumetric methane uptake for HKUST-1 when ideal crystal density is assumed[5]. When applying pressures in the range of 6.9 to 68.9 MPa to densify powdered HKUST-1 in previous works[5], the MOF density increased but the total pore volume was reduced due to partial collapse of the MOF structure. As a result, the methane capacity was increased only up to 180 cm^3 (STP) cm^{-3} (that is, a 35% loss instead of the theoretical value without collapse). Overall, we found that $_{mono}$HKUST-1 shows an enhancement of the methane adsorption capacity of, at least, about 99% over previous reported experimental values on a powder, and 45% on a densified powder. Taking into account previous accurate computational models for methane storage[8], we reasonably believe this value to be, within a small range of statistical error, the physical limit of ambient temperature methane storage capacity in porous materials.

Very often, densification of strictly microporous materials comes at the expense of slower adsorption kinetics. We have measured the kinetics for methane adsorption, and the evolution of the pressure decay with time, in $_{powd}$HKUST-1 and $_{mono}$HKUST-1 samples at 5, 10, 20, 40 and 60 bar (Fig. 3c,d). Interestingly, we noticed no important differences in the adsorption kinetics between the two samples, showing very fast equilibrium between 75 and 200 s for both $_{powd}$HKUST-1 and $_{mono}$HKUST-1. Small differences are due to the absence of mesoporosity in $_{mono}$HKUST-1, and therefore slightly slower transport diffusivity compared with the nanometre-sized particles of $_{powd}$HKUST-1.

In addition to the DOE targets described above, the Advanced Research Projects Agency-Energy (ARPA-E) has also set the methane deliverable capacity to 315 cm^3 (STP) cm^{-3}, where the deliverable capacity is defined as the uptake at the storage pressure of 65 bar minus the uptake at the depletion pressure of 5.8 bar. This ARPA-E methane deliverable target is often considered too high to be reached[29,30]. Indeed, current theoretical—using crystal density—maximum delivery capacities of top-performing adsorbents are around 200 cm^3 (STP) cm^{-3}: for example, 190, 208, 183 and 180 cm^3 (STP) cm^{-3} for HKUST-1 (ref. 5), MOF-519 (ref. 31), NU-125 (ref. 5), and MOF-905 (ref. 32), respectively, among others[29,30]. Taking into account previous packing losses due to MOF densification, all these delivery capacities are in practice likely to

decrease to about 135 cm^3 (STP) cm^{-3}, assuming a typical 35% packing loss[2]. Our $_{mono}$HKUST-1 shows a delivery capacity, using the real bulk density, of 172 cm^3 (STP) cm^{-3} (that is, the difference between 259 and 87 cm^3 (STP) cm^{-3}, for the uptakes obtained at 65 and 5.8 bar, respectively). Again, to the best of our knowledge, this is the highest deliverable capacity achieved by any adsorbent after successful pelletization and shaping.

To design a material for adsorption applications, the volumetric capacity of a material is not the only element that needs to be taken into consideration. Heat management due to the exo/endothermic nature of the ad/desorption phenomena, as well as efficient packing of a monolith in a tank, impurity tolerance (for example, the presence of C_2H_6, H_2O), recyclability (100 cycles) and cost of adsorbent (<US$10 kg^{-1}) need to be optimized when looking at the DOE targets[4,33]. In the case of $_{mono}$HKUST-1, the three times higher density compared with that of the powder is expected to improve heat transfer significantly[34–36]. Moreover, the generic approach of the sol–gel synthesis also allows for doping with materials with higher heat conductivity[37,38]. At the same time, one-stage sol–gel synthesis is flexible enough to be used to shape the monolith with the required morphology to be packed efficiently in a tank so space can be used efficiently[39].

Mechanical properties

Once a MOF has been shaped and densified, one of the main challenges that pellets and monolithic structures need to face in industrial settings is the necessity to support mechanical stress from, for example, friction against the tank walls, vibrations within a column, the weight of the adsorbent, and external pressurization. To determine the mechanical properties of the synthesized $_{mono}$HKUST-1, we have measured the elastic modulus and hardness of the monolithic samples using a nanoindentation technique (Fig. 4), and compared them with theoretical calculations[40]. Our results show that the indentation modulus (I) of $_{mono}$HKUST-1 is 11.5 ± 0.4 GPa (Supplementary Fig. 13), from which we established its Young's modulus (E) to be 9.3 ± 0.3 GPa (taking Poisson's ratio, $\nu = 0.433$ from Woll *et al.*)[41]. Interestingly, our current Young's modulus is ∼15% higher than that recently predicted by density functional theory (DFT, $E = 8.1$ GPa) (ref. 40) for an isotropic polycrystalline HKUST-1 where its isotropic $\nu = 0.45$. Another revealing comparison can be made against the mechanical properties of an epitaxially grown HKUST-1 polycrystalline film by Woll *et al.* (that is, $E = 9.3$ GPa, $H = 198 \pm 19$ MPa) (ref. 41), also measured by a nanoindentation method. Most remarkably, although the Young's modulus of our $_{mono}$HKUST-1 matches the conventional HKUST-1 (see above)[41], the mechanical hardness of $_{mono}$HKUST-1 ($H = 460 \pm 30$ MPa) in fact surpasses that of its conventional counterpart by more than 130%. Significantly, this means that the monolithic version of HKUST-1 has improved mechanical durability against permanent plastic deformation, simply ascribed to its high bulk density (Table 1). Likewise, $_{mono}$HKUST-1 will have a significantly greater yield strength (σ_Y), because $\sigma_Y \propto H$ (ref. 42). Indeed we have carried out atomic force microscopy (AFM) imaging of the residual indents, verifying their good resistance against surface cracking, as evidenced in Fig. 4d. In addition to providing high mechanical strength, the high bulk density of the monolith could also lead to higher thermal conductivity, providing further benefits in practical applications.

Outlook for gas storage applications

In conclusion, we have synthesized monolithic MOF, $_{mono}$HKUST-1, using a sol–gel process without requiring binders and/or high pressures. The mild conditions of the synthetic protocol and soft drying process lead to a dense monolithic structure. Small primary particles and only a mild drying process are necessary to allow the successful synthesis. $_{mono}$HKUST-1 was able to retain the characteristic structure and porosity of the powder, while showing a three times higher density and therefore volumetric gas adsorption capacity. $_{mono}$HKUST-1 showed an outstanding methane capacity of 259 cm^3 (STP) cm^{-3} at 65 bar, becoming the first conformed adsorbent, after successful densification and shaping, to achieve the volumetric DOE target (that is, 263 cm^3 (STP) cm^{-3}). Taking into account earlier accurate computational models for methane storage, we reasonably believe this value to be, within a very small range of statistical error, the physical limit of ambient temperature methane storage capacity in porous materials. From the mechanical point of view, it is striking to discover that the hardness of $_{mono}$HKUST-1 exceeds twice that of any conventional HKUST-1 material published to date. Although further engineering of the monolithic material is required to efficiently pack it in a tank and to deal with heat management, this work represents a significant step forward in the shaping and densification of MOFs. We believe it opens the gate towards their applicability in ANG and other real-world industrial applications where high volumetric adsorption capacities and resilient mechanical properties are critical.

Methods

Methods, including statements of data availability and any associated accession codes and references, are available in the online version of this paper.

Received 27 July 2016; accepted 2 November 2017; published online 11 December 2017

References

1. Makal, T. A., Li, J.-R., Lu, W. & Zhou, H.-C. Methane storage in advanced porous materials. *Chem. Soc. Rev.* **41,** 7761–7779 (2012).
2. Mason, J. A. *et al*. Methane storage in flexible metal–organic frameworks with intrinsic thermal management. *Nature* **527,** 357–361 (2015).
3. Schoedel, A., Ji, Z. & Yaghi, O. M. The role of metal–organic frameworks in a carbon-neutral energy cycle. *Nat. Energy* **1,** 16034 (2016).
4. He, Y., Zhou, W., Qian, G. & Chen, B. Methane storage in metal–organic frameworks. *Chem. Soc. Rev.* **43,** 5657–5678 (2014).
5. Peng, Y. *et al*. Methane storage in metal–organic frameworks: current records, surprise findings, and challenges. *J. Am. Chem. Soc.* **135,** 11887–11894 (2013).
6. Alezi, D. *et al*. MOF crystal chemistry paving the way to gas storage needs: aluminum-based soc-MOF for CH_4, O_2, and CO_2 storage. *J. Am. Chem. Soc.* **137,** 13308–13318 (2015).
7. Moghadam, P. Z. *et al*. Development of a Cambridge Structural Database subset: a collection of metal–organic frameworks for past, present, and future. *Chem. Mater.* **29,** 2618–2625 (2017).
8. Wilmer, C. E. *et al*. Large-scale screening of hypothetical metal–organic frameworks. *Nat. Chem.* **4,** 83–89 (2012).
9. Chung, Y. G. *et al*. Computation-ready, experimental metal–organic frameworks: a tool to enable high-throughput screening of nanoporous crystals. *Chem. Mater.* **26,** 6185–6192 (2014).
10. Mason, J. A., Veenstra, M. & Long, J. R. Evaluating metal–organic frameworks for natural gas storage. *Chem. Sci.* **5,** 32–51 (2014).
11. Casco, M. E. *et al*. High-pressure methane storage in porous materials: are carbon materials in the pole position? *Chem. Mater.* **27,** 959–964 (2015).
12. Tian, T., Velazquez-Garcia, J., Bennett, T. D. & Fairen-Jimenez, D. Mechanically and chemically robust ZIF-8 monoliths with high volumetric adsorption capacity. *J. Mater. Chem. A* **3,** 2999–3005 (2015).
13. Bueken, B. *et al*. Gel-based morphological design of zirconium metal-organic frameworks. *Chem. Sci.* **8,** 3939–3948 (2017).
14. Tan, G., John, V. T. & McPherson, G. L. Nucleation and growth characteristics of a binary low-mass organogel. *Langmuir* **22,** 7416–7420 (2006).
15. Fairén-Jiménez, D., Carrasco-Marín, F. & Moreno-Castilla, C. Inter-and intra-primary-particle structure of monolithic carbon aerogels obtained with varying solvents. *Langmuir* **24,** 2820–2825 (2008).
16. Fairen-Jimenez, D. *et al*. Surface area and microporosity of carbon aerogels from gas adsorption and small-and wide-angle X-ray scattering measurements. *J. Phys. Chem. B* **110,** 8681–8688 (2006).
17. Pekala, R. Organic aerogels from the polycondensation of resorcinol with formaldehyde. *J. Mater. Sci.* **24,** 3221–3227 (1989).
18. Dorcheh, A. S. & Abbasi, M. Silica aerogel; synthesis, properties and characterization. *J. Mater. Process. Technol.* **199,** 10–26 (2008).

19. Horcajada, P. *et al*. Colloidal route for preparing optical thin films of nanoporous metal–organic frameworks. *Adv. Mater.* **21,** 1931–1935 (2009).
20. Li, L. *et al*. A synthetic route to ultralight hierarchically micro/mesoporous Al (III)-carboxylate metal-organic aerogels. *Nat. Commun.* **4,** 1774 (2013).
21. Kim, K.-J. *et al*. High-rate synthesis of Cu–BTC metal–organic frameworks. *Chem. Commun.* **49,** 11518–11520 (2013).
22. Getzschmann, J. *et al*. Methane storage mechanism in the metal-organic framework $Cu_3(btc)_2$: An *in situ* neutron diffraction study. *Microporous Mesoporous Mater.* **136,** 50–58 (2010).
23. Nune, S. K. *et al*. Synthesis and properties of nano zeolitic imidazolate frameworks. *Chem. Commun.* **46,** 4878–4880 (2010).
24. Cravillon, J. *et al*. Rapid room-temperature synthesis and characterization of nanocrystals of a prototypical zeolitic imidazolate framework. *Chem. Mater.* **21,** 1410–1412 (2009).
25. Pan, Y., Liu, Y., Zeng, G., Zhao, L. & Lai, Z. Rapid synthesis of zeolitic imidazolate framework-8 (ZIF-8) nanocrystals in an aqueous system. *Chem. Commun.* **47,** 2071–2073 (2011).
26. Sánchez-Sánchez, M. *et al*. Synthesis of metal–organic frameworks in water at room temperature: salts as linker sources. *Green Chem.* **17,** 1500–1509 (2015).
27. Lemmon, E. W., McLinden, M. O. & Friend, D. G. Thermophysical Properties of Fluid Systems. in *NIST Chemistry WebBook, NIST Standard Reference Database Number 69* (eds Linstrom, P. J. & Mallard, W. G.) (National Institute of Standards and Technology, 2005).
28. Fairen-Jimenez, D. *et al*. Understanding excess uptake maxima for hydrogen adsorption isotherms in frameworks with rht topology. *Chem. Commun.* **48,** 10496–10498 (2012).
29. Gómez-Gualdrón, D. A., Wilmer, C. E., Farha, O. K., Hupp, J. T. & Snurr, R. Q. Exploring the limits of methane storage and delivery in nanoporous materials. *J. Phys. Chem. C* **118,** 6941–6951 (2014).
30. Simon, C. M. *et al*. The materials genome in action: identifying the performance limits for methane storage. *Energy Environ. Sci.* **8,** 1190–1199 (2015).
31. Gándara, F., Furukawa, H., Lee, S. & Yaghi, O. M. High methane storage capacity in aluminum metal–organic frameworks. *J. Am. Chem. Soc.* **136,** 5271–5274 (2014).
32. Jiang, J., Furukawa, H., Zhang, Y.-B. & Yaghi, O. M. High methane storage working capacity in metal–organic frameworks with acrylate links. *J. Am. Chem. Soc.* **138,** 10244–10251 (2016).
33. Methane Opportunities for Vehicular Energy (MOVE). DE-FOA-0000672, February 22, 2012. https://arpa-e-foa.energy.gov
34. Wang, L. W. *et al*. Study of thermal conductivity, permeability, and adsorption performance of consolidated composite activated carbon adsorbent for refrigeration. *Renew. Energy* **36,** 2062–2066 (2011).
35. Huang, B. L. *et al*. Thermal conductivity of a metal-organic framework (MOF-5): Part II. Measurement. *Int. J. Heat Mass Transfer* **50,** 405–411 (2007).
36. Jeremias, F., Henninger, S. K. & Janiak, C. High performance metal-organic-framework coatings obtained via thermal gradient synthesis. *Chem. Commun.* **48,** 9708–9710 (2012).
37. Ahn, H. S. *et al*. Enhanced heat transfer is dependent on thickness of graphene films: the heat dissipation during boiling. *Sci. Rep.* **4,** 6276 (2014).
38. Zhou, M. *et al*. Highly conductive porous graphene/ceramic composites for heat transfer and thermal energy storage. *Adv. Funct. Mater.* **23,** 2263–2269 (2013).
39. Danks, A. E., Hall, S. R. & Schnepp, Z. The evolution of 'sol–gel' chemistry as a technique for materials synthesis. *Mater. Horiz.* **3,** 91–112 (2016).
40. Ryder, M. R., Civalleri, B., Cinque, G. & Tan, J.-C. Discovering connections between terahertz vibrations and elasticity underpinning the collective dynamics of the HKUST-1 metal–organic framework. *CrystEngComm* **18,** 4303–4312 (2016).
41. Bundschuh, S. *et al*. Mechanical properties of metal-organic frameworks: an indentation study on epitaxial thin films. *Appl. Phys. Lett.* **101,** 101910 (2012).
42. Tabor, D. Indentation hardness: fifty years on a personal view. *Phil. Mag. A* **74,** 1207–1212 (1996).

Acknowledgements

This project has received funding from the European Research Council (ERC) under the European Union's Horizon 2020 research and innovation programme (NanoMOFdeli), ERC-2016-COG 726380, and the EPSRC IAA Partnership Development Award (RG/75759). D.F.-J. thanks the Royal Society for funding through a University Research Fellowship. J.C.T. would like to acknowledge the EPSRC (EP/N014960/1) for research funding. G.D. and P.A.M. acknowledge financial support from the EU under grant numbers 312483 ESTEEM2 and 291522 3DIMAGE. J.S.A. acknowledges financial support from MINECO (MAT2016-80285-p), H2020 (MSCA-RISE-2016/Nanomed Project) and GV (PROMETEOII/2014/004).

Author contributions

T.T. and D.F.-J. designed the research. T.T. performed the materials synthesis and characterization, and D.V. carried out the N_2 gas adsorption, both under the supervision of D.F.-J. M.E.C. and J.S.-A. participated in the characterization of the materials, including high-pressure adsorption tests and TGA–MS; Z.Z. performed the nanoindentation experiments under the supervision of J.-C.T.; G.D. carried out the TEM analysis under the supervision of P.A.M.; T.T., P.Z.M. and D.J.-F. wrote the first draft of the manuscript with input from the rest of the authors. All the authors contributed to the final version.

Additional information

Supplementary information is available in the online version of the paper. Reprints and permissions information is available online at www.nature.com/reprints. Publisher's note: Springer Nature remains neutral with regard to jurisdictional claims in published maps and institutional affiliations. Correspondence and requests for materials should be addressed to D.F.-J.

Competing financial interests

T.T. and D.F.-J. have financial interest in the start-up company Immaterial Labs, which is seeking to commercialize metal–organic frameworks.

Methods

Materials. $Cu(NO_3)_2 \cdot 2.5H_2O$ (98%), BTC (95%), ethanol (≥99.5%) and silicone oil (density = 0.967 g ml^{-1} at 20 °C) were purchased from Sigma Aldrich and used as received.

Synthesis of HKUST-1 samples. $_{mono}$HKUST-1 was synthesized based on a modification of the synthesis method of HKUST-1 reported by Wee and colleagues[43]. Solutions of BTC (10 ml, 0.062 M) and $Cu(NO_3)_2 \cdot 2.5H_2O$ (10 ml, 0.064 M) in ethanol were mixed and stirred for 10 min at room temperature (20 ± 1 °C). After centrifugation, the solid was kept in the Falcon tube and washed in ethanol for 10 min (15 ml, 3 times) and then dried in an incubator at room temperature (20 ± 1 °C) overnight. The solid was then transferred to a glass vial and was further dried at 120 °C in an incubator under vacuum overnight. $_{powd}$HKUST-1 was obtained by drying the washed solid after centrifugation, at high temperature (120 °C) rather than allowing them to dry first at room temperature. The yields of $_{mono}$HKUST-1 and $_{powd}$HKUST-1 were 53% after activation. Two samples of HKUST-1 with larger particle size were synthesized following the previous method but at 40 °C and 60 °C. The yields were 53% and 55%, respectively, after activation. These new samples were dried at different temperatures from 20 to 80 °C to provide either a powder or a monolithic sample.

Characterization of $_{mono}$HKUST-1. Powder X-ray diffraction (PXRD) patterns were recorded with a Bruker D8 diffractometer using CuKα_1 (λ = 1.5405 Å) radiation with a step of 0.02° at a scanning speed of 8 s per step. IR was performed on a PerkinElmer Spectrum 100 FT-IR spectrometer. Scanning electron microscope (SEM) images were taken using a FEI XL30 FEGSEM with an accelerating voltage of 5 kV. TEM was carried out using a FEI Osiris S/TEM operated at 200 kV, operated in scanning mode. Elemental analysis in the TEM was performed with a Bruker Super-X EDX detector. The C, H, N analysis was performed on an Exeter Analytical CE 440 elemental analyser at a combustion temperature of 975 °C while Cu analysis was performed on a Thermo Scientific iCAP 7400 ICP-OES analyser against 1 ppm and 10 ppm standards. Thermogravimetric analysis–mass spectrometry (TGA–MS) was performed using TGA Q500 from TA Instruments in nitrogen, from room temperature to 900 °C, using a ramp rate of 5 °C min^{-1}. An additional TGA–MS was performed using a ramp rate of 5 °C min^{-1} up to 120 °C, keeping the sample for 8 h at this temperature, and then heated again (ramp rate of 5 °C min^{-1}) up to 900 °C.

N_2 adsorption isotherms were undertaken at 77 K using a Micromeritics 3Flex instrument. High-pressure methane adsorption at 298 K was conducted using an HPVA II High Pressure Volume Analyser from Micromeritics. Adsorption kinetics for methane were measured at different pressures by recording the manifold pressure versus time until equilibrium was reached. The temperature was controlled by using a Julabo F25 HE bath circulator. Prior to the analyses, the samples were activated overnight at 120 °C (vacuum) before measuring the mass, and then degassed *in situ* thoroughly before the gas adsorption.

Mercury porosimetry was obtained up to a final pressure of 2,000 bar using an AutoPore IV 9500 instrument from Micromeritics. This technique was used to estimate the particle density of the $_{mono}$HKUST-1 at atmospheric pressure. Prior to the analysis, all samples were activated overnight at 120 °C (vacuum) before measuring the mass, and then degassed *in situ* thoroughly before the mercury porosimetry. Full details and discussion on density evaluation are included in the Supplementary Information, page S9.

The nanoindentation study was performed using an MTS Nanoindenter XP instrument, equipped with a continuous stiffness measurement module. HKUST-1 monoliths were mounted on an epoxy resin (Struers Epofix) and the surface was carefully prepared using an established methodology designed for studying MOF crystals[44]. The prepared monolith surface (Fig. 4c) was cleaned with isopropanol and then desolvated at 100 °C. The evacuated sample was secured in a desiccator until testing. A Berkovich diamond tip was used to measure load–displacement data to a surface penetration depth of 2,000 nm, from which the hardness values and Young's moduli were derived in accordance with the Oliver–Pharr method[45].

Data availability. The experimental dataset generated and/or analysed during the current study are available from the corresponding author on reasonable request.

References

43. Wee, L. H., Lohe, M. R., Janssens, N., Kaskel, S. & Martens, J. A. Fine tuning of the metal–organic framework $Cu_3(BTC)_2$ HKUST-1 crystal size in the 100 nm to 5 micron range. *J. Mater. Chem.* **22,** 13742–13746 (2012).
44. Tan, J. C., Bennett, T. D. & Cheetham, A. K. Chemical structure, network topology, and porosity effects on the mechanical properties of zeolitic imidazolate frameworks. *Proc. Natl Acad. Sci. USA* **107,** 9938–9943 (2010).
45. Tan, J. C., Merrill, C. A., Orton, J. B. & Cheetham, A. K. Anisotropic mechanical properties of polymorphic hybrid inorganic–organic framework materials with different dimensionalities. *Acta Mater.* **57,** 3481–3496 (2009).